Research Article | Vol. 12, No. 10 / 1 Oct 2021 / Biomedical Optics Express 6545
Biomedical Optics EXPRESS

Label-free skin penetration analysis using time-resolved, phase-modulated stimulated Raman scattering microscopy

TERUMASA ITO,[1,2,*] RISA IGUCHI,[3] FUMIAKI MATSUOKA,[1,2] YOJI NISHI,[3] TSUYOSHI OGIHARA,[3] AND KAZUHIKO MISAWA[1,2]

[1] *Department of Applied Physics, Tokyo University of Agriculture and Technology, 2-24-16 Naka-cho, Koganei, Tokyo 184-8588, Japan*
[2] *Department of Biomedical Engineering, Tokyo University of Agriculture and Technology, 2-24-16 Naka-cho, Koganei, Tokyo 184-8588, Japan*
[3] *Matsumoto Trading Co., Ltd., 1-13-7 Nihonbashi-Muromachi, Chuo-ku, Tokyo 103-0022, Japan*
[*] *teru-ito@cc.tuat.ac.jp*

Abstract: Skin penetration analysis of topically applied drugs or active compounds is essential in biomedical applications. Stimulated Raman scattering (SRS) microscopy is a promising label-free skin penetration analysis tool. However, conventional SRS microcopy suffers from limited signal contrast owing to strong background signals, which prevents its use in low-concentration drug imaging. Here, we present a skin penetration analysis method of topical agents using recently developed phase-modulated SRS (PM-SRS) microscopy. PM-SRS uses phase modulation and time-resolved signal detection to suppress both nonlinear background signals and Raman background signals from a tissue. A proof-of-concept experiment with a topically applied skin moisturizing agent (ectoine) in an *in vitro* skin tissue model revealed that PM-SRS with 1.7-ps probe delay yields a signal contrast 40 times higher than that of conventional amplitude-modulated SRS (AM-SRS). Skin penetration measurement of a topical therapeutic drug (loxoprofen sodium) showed that the mean drug concentration at the tissue surface layer after 240 min was 47.3 ± 4.8 mM. The proposed PM-SRS microscopy can be employed to monitor the spatial and temporal pharmacokinetics of small molecules in the millimolar concentration regime.

1. Introduction

The current focus of dermatological, pharmaceutical, and cosmetic research and development is on the skin penetration of topically applied chemicals [1–3]. Testing the skin penetration of target molecules is an essential step in the early-stage screening of topical drugs and skincare-product development. The data obtained from penetration analysis would advance our understanding of the efficacy of topical drugs and skin care formulations or the risk of potentially toxic ingredients.

Skin is an effective barrier that protects living organisms from environmental, physical, and chemical stresses. The barrier function resides primarily in the stratum corneum (SC), a superficial layer of the epidermis composed of cornified keratinocytes surrounded by multilamellar lipid membranes. This layer acts as the first line of defense against the entry of extraneous chemicals. Penetration through the skin barrier is generally complex and difficult to predict because it depends on numerous factors, such as physicochemical properties of substances (molecular weight and lipophilicity), the formulation used, the anatomical site of application, and the physiological state of the skin [3]. Therefore, a rapid, quantitative test platform for analyzing skin penetration is highly desirable.

Conventional analytical approaches include tape stripping [4], Franz diffusion cells [5], and confocal Raman microscopy [6,7]. Tape stripping, which sequentially removes SC layers with

#436142 https://doi.org/10.1364/BOE.436142
Journal © 2021 Received 12 Jul 2021; revised 6 Sep 2021; accepted 6 Sep 2021; published 24 Sep 2021

Biomedical Optics EXPRESS

adhesive tape, is a well-established method to examine the localization of substances. Although this technique enables depth profiling, it is destructive and, therefore, cannot be employed directly to monitor the transport of substances at the same position. The Franz cell diffusion method, an *in vitro* skin permeation assay, is widely employed to predict the diffusion kinetics of applied chemicals. However, it lacks spatial resolution to analyze the microscopic localization of substances in tissues. Confocal Raman microscopy has been recognized as a powerful tool for analyzing skin penetration because it provides non-destructive depth-profiling capabilities with micrometer-scale spatial resolution. In addition, this analysis technique allows direct chemical analysis based on label-free vibrational spectroscopy, without perturbing the pharmacokinetics and physiological activities of small molecules. Nevertheless, because confocal Raman microscopy relies on the weak signal generated via the spontaneous Raman scattering process, it typically requires a long data acquisition time; thus, it does not support real-time depth imaging.

As solutions to the speed limitation, coherent Raman scattering microscopy methods such as coherent anti-Stokes Raman scattering (CARS) [8–10] and stimulated Raman scattering (SRS) [11–15] have attracted increasing attention. These nonlinear microscopy techniques offer amplification of the Raman signal by several orders of magnitude via coherent excitation of molecular vibrations using ultrashort laser pulses, enabling real-time chemical imaging in a purely non-labeled manner. CARS and SRS microscopy have been applied to the imaging of topically applied drugs and active compounds [11,14,15].

Despite these advantages, quantitative skin penetration measurement techniques using conventional coherent Raman microscopy remain challenging, especially when the local chemical concentration in the tissue is in the practical range (typically tens of millimolar or less). This is because the weak signal of the target chemical is often shadowed by strong background signals. In CARS microscopy, the non-resonant background signal interferes with and distorts the Raman spectrum of the sample [9,16]. Conventional amplitude-modulated SRS (AM-SRS) microscopy is also affected by nonlinear background signals generated via other competing nonlinear pump–probe processes [17,18]. In addition, SRS signals from major intrinsic biomolecules in a tissue, such as lipids, proteins, and water, are considered as background signals, which inevitably overlap with the weak signals of interest. Thus, conventional coherent Raman microscopy that probes a single vibrational frequency suffers from a limited signal contrast, which prevents it from being used for practical skin penetration analysis. To overcome this limitation, we recently developed phase-modulated SRS (PM-SRS) microscopy [19,20]. The principle of this new imaging method is to remove background signals using phase modulation and time-resolved detection. Previous work has shown that AM-induced nonlinear background signals can be removed using PM heterodyne detection of vibrational signals. Moreover, the background Raman signals from a tissue can also be suppressed by time-resolved SRS signal detection with tailored pump and probe pulses. However, the detectability of the new microscopy technique for low-concentration drug imaging applications has not been demonstrated.

In this study, we report a label-free, depth-resolved SRS imaging technique of topical skin agents in an *in vitro* skin tissue model. We show that PM-SRS microscopy satisfies the requirements for a practical skin penetration analysis: (i) quantitative measurement capability (enhanced signal contrast) and (ii) high detectability (a low limit of detection) without using any labeled tracers. As a proof-of-concept experiment, we first present the skin penetration measurement of a skin moisturizing agent in an aqueous solution. Our focus here is on comparing the signal contrast of PM-SRS with that of conventional AM-SRS in spectroscopy and imaging experiments, highlighting the advantages of PM-SRS for quantitative chemical measurements in a tissue. To further demonstrate the high detectability of the PM-SRS microscopy, we observed the penetration profiles of a topically applied local anesthetic drug and a nonsteroidal anti-inflammatory drug. We show that the diffusion kinetics of these drug molecules in the skin tissue model can be continuously monitored in the millimolar concentration regime.

Biomedical Optics EXPRESS

2. Methods

Figure 1(a) illustrates the setup of skin penetration measurement based on SRS microscopy. The donor aqueous solution sample was applied to an *in vitro* three-dimensional (3D) skin tissue model (Epiderm Epi-606X, Mattek) placed on a microscope glass slide. The receiver solution (1× phosphate saline buffer) was filled under the tissue to facilitate penetration (see Supplement 1 for details). SRS microscopy provides depth-resolved vibrational signal contrast via the nonlinear optical effect at the tightly focused beam spot. A two-dimensional (2D) depth image was acquired by raster scanning of the sample stage along the *XZ* direction. To analyze skin penetration based on SRS imaging, the distribution of the target molecules (the chemical map) needs to be drawn on the corresponding tissue structure data. In addition, the sample deformation or drift must be monitored during time-lapse imaging for accurate depth-profiling analysis. To address these requirements, confocal-reflection imaging is used to capture the layered structure of the skin tissue model, and the SRS image is superimposed on the confocal-reflection image, as shown in Fig. 1(a).

The microscopy system offers two SRS microscopy modes—the AM-SRS mode (Fig. 1(b)) and the PM-SRS mode (Fig. 1(c)). The principles of the two SRS methods have been described elsewhere [19] and in Supplement 1. A clear advantage of the PM-SRS over the AM-SRS is its superior background suppression capability. Through PM heterodyne signal detection, the PM-SRS rejects background signals due to competing nonlinear effects in AM-SRS, such as cross-phase modulation. Moreover, PM-SRS suppresses the Raman background signals with a short coherence lifetime from tissue components such as proteins and lipids. This feature can be understood by focusing on the difference in the excitation and detection processes of the two SRS microscopies in the time domain. In the AM-SRS, both excitation and detection of molecular vibrations are provided by two pulses (pump and Stokes). In the PM-SRS mode, however, these processes are temporally separated and the molecular vibration initiated by an impulsive pump/Stokes excitation pulse is heterodyne-detected using a pair of temporally delayed probe pulses (the PM probe and the local oscillator (LO) probe). The time-resolved signal detection with time-asymmetric probe pulses, which are delayed typically by 0.5−2.0 ps with respect to the impulsive pump/Stokes pulse, enhances the specific molecular vibrations with a long coherence lifetime. Therefore, PM-SRS suppresses the broadband (short-lived) spectral background signals from unwanted tissue Raman scattering and selectively detects the target narrowband (long-lived) signal with a superior signal-to-background ratio (S/B).

Figure 1(d) shows the optical setup of the dual AM-/PM-SRS microscope (Supplement 1). A near-infrared broadband pulse generated by a Ti:sapphire oscillator (Vitara, Coherent) was split into three pulses (P0, P1, and P2). The P1 pulse was phase-modulated in the PM mode, and the P2 pulse was amplitude-modulated in the AM mode. The pulse shaper, consisting of chirped mirrors and a 4f-optics with a spatial light modulator, produces a femtosecond P0 pulse (~15 fs) for impulsive excitation used in the PM mode. Strong linear and nonlinear chirps are added to the P1 and P2 pulses to stretch and shape them to be temporally asymmetric picosecond pulses (rise time: 0.4 ps, fall time: 1.9 ps), providing a fine spectral resolution of ~25 cm^{-1} via spectral-focusing [20]. The combined beams were focused onto the sample using an objective lens with NA = 0.50. After the sample, the P0 excitation pulse was blocked using a crossed polarizer. The LO beam transmitted through the sample I_{LO} contained a weakly intensity-modulated signal ΔI generated via SRS. The output signal on the LO, which is proportional to the concentration of the target chemical compound, was detected by a photodiode and demodulated by a lock-in amplifier. The microscopic system can be switched between the two SRS modes by turning the impulsive excitation pulse on and off, driving either the amplitude or phase modulator, and selecting a detection filter that blocks the P2 and P1 pulses, respectively. The parameters for each detection mode are presented in Table 1.

Biomedical Optics EXPRESS

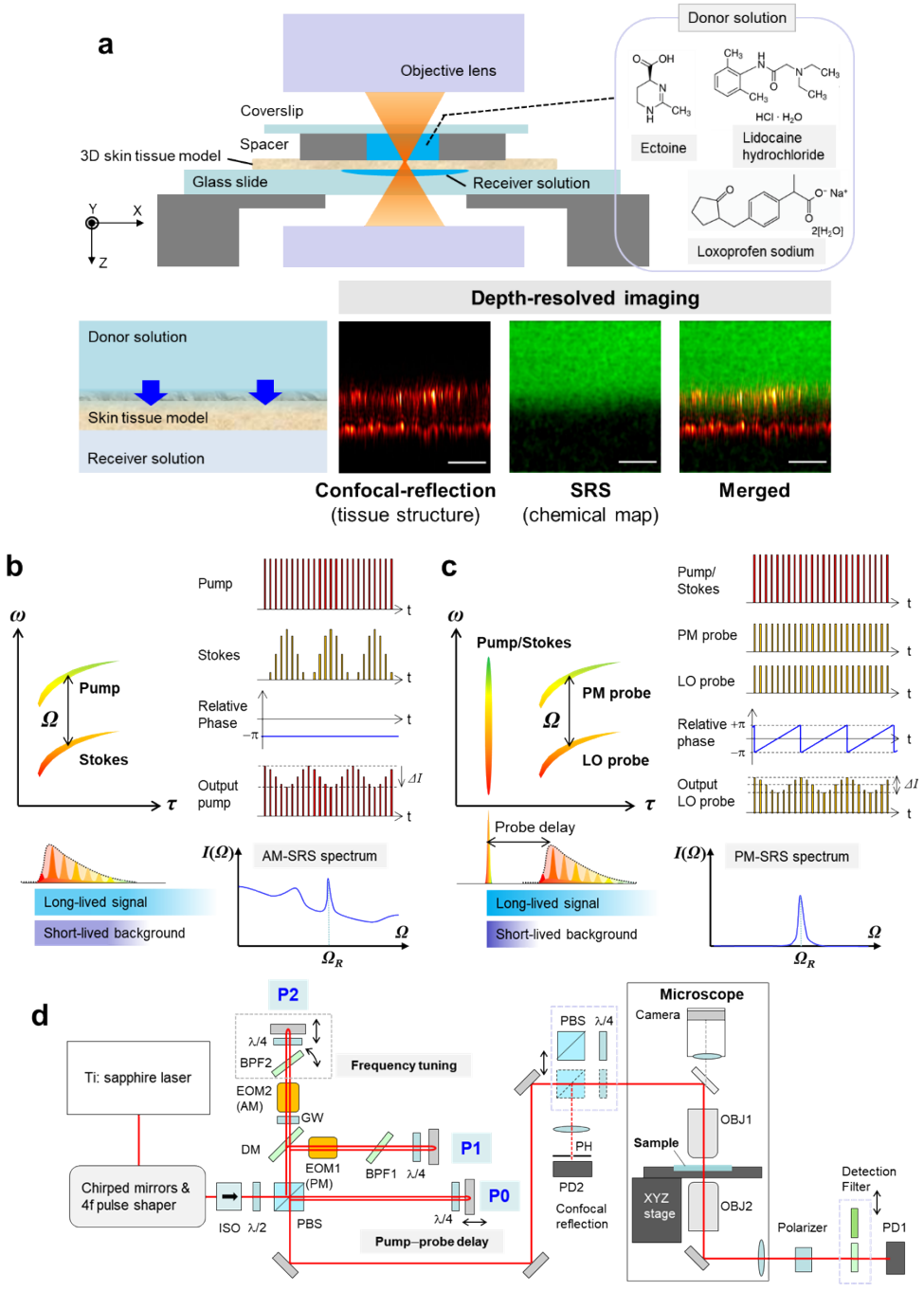

Fig. 1. Skin penetration test platform based on SRS microscopy. (a) Schematic illustration of the experimental setup. (b)-(c) The process of (b) AM-SRS and (c) PM-SRS, where the diagram of frequency (ω) vs. group delay (τ) and the corresponding temporal pulse shape (left), the RF modulation scheme (upper right), and a typical spectrum (bottom right) are illustrated, respectively. (d) Optical layout of the dual AM-SRS/PM-SRS microscopy system (ISO: optical isolator, BPF: bandpass filter, PBS: polarizing beam splitter, λ/2: half waveplate, λ/4: quarter waveplate, EOM1: PM-electro-optic modulator, EOM2: AM-electro-optic modulator, DM: dichroic mirror, GW: glass window, OBJ: objective lens, PD1 and PD2: photodiodes, PH: pinhole). For confocal-reflection imaging, a PBS and a quarter waveplate were inserted on the beam path in front of the entrance of the microscope. The beam paths of the AM-SRS, PM-SRS and confocal-reflection microscopy modes are illustrated in Fig. S1.

Biomedical Optics EXPRESS

Table 1. Detection modes and parameters of the SRS microscope

Detection mode	P0 pulse (femtosecond)	P1 pulse (picosecond)	P2 pulse (picosecond)	Detection filter	Pump–probe delay
AM-SRS	--	Pump (LO)	Stokes (AM: 1 MHz sinusoidal)	Bandpass, blocking P2	Zero
PM-SRS	Pump/Stokes (impulsive)	PM probe (PM: 100 kHz sawtooth)	LO probe	Long-pass, blocking P1	Tunable

In confocal-reflection imaging, the backscattered light from the tissue is collected and detected using the confocal detection unit in front of the microscope entrance (a polarizing beam splitter and a quarter waveplate are inserted on the beam path). In the 3D skin tissue model, a strong confocal-reflection signal is observed at the middle of the SC layer and the liquid–tissue interface at the bottom tissue, respectively, owing to the large mismatch in refractive indices. These signals are used to identify the thickness and local microstructure of the tissue (Fig. S2).

3. Results

3.1. High-contrast depth imaging of a skin moisturizing agent by PM-SRS

First, to show the performance of quantitative measurement of the PM-SRS, we examined the penetration of ectoine, an amino acid derivative widely utilized as a skin moisturizing agent, using an *in vitro* skin tissue model. Here, we focus on comparing the signal contrast of the PM-SRS with that of the conventional AM-SRS. The vibrational spectra of 10% aqueous ectoine solution and pure water acquired with the two different SRS modes are compared in Fig. 2(a). The AM-SRS spectrum includes intense background signals generated by the AM-induced nonlinear effects (primarily due to cross-phase modulation). The S/B of the AM-SRS at the most prominent Raman peak ($C–COO^-$ stretching vibration at 848 cm^{-1}) was less than unity (~0.68) despite the high concentration. In contrast, the spectrum obtained via the PM-SRS mode exhibited an enhanced peak at 848 cm^{-1} with a flat background signal baseline close to the zero level. Thus, the PM-SRS signal was proportional to the ectoine concentration (Fig. 2(b)), which enabled image-based chemical measurements without offset correction.

The high-contrast feature of the PM-SRS can be highlighted in tissue imaging. Figure 2(c) shows the PM-SRS images acquired 15 min, 60 min, and 180 min after applying the 10% ectoine solution, respectively, and Fig. 2(d) shows the AM-SRS image acquired after 180 min. Each SRS image is superimposed over the confocal-reflection image to aid the visualization of the layer structure. The changes in the surface position and thickness, presumably due to sample drift and deformation, were visible in the confocal-reflection image. The probe delay time in the PM-SRS imaging was set to be 1.7 ps to balance the S/B and sensitivity (Fig. S6). The AM-SRS image clearly lacks the vibrational signal contrast even in the vicinity of the superficial SC layer, whereas the PM-SRS images display a high-contrast 2D distribution of ectoine without being affected by the background signals. Figure 2(e) shows a PM-SRS image at 848 cm^{-1} with a blank (0%) donor solution. The control experiment verified that the tissue Raman background signal was removed using the delayed probe pulses. The S/B in the skin penetration experiment is defined as the SRS signal in the donor solution divided by the mean tissue background signal at the upper SC layer. In the tissue imaging of ectoine, the S/B of the AM-SRS image was 0.40, whereas that of the PM-SRS image was 16; thus, PM-SRS provided a 40 times higher signal contrast. The results suggest that PM-SRS microscopy can be used to depict a quantitative concentration map in a tissue. The time-lapse PM-SRS images shown in Fig. 2(c) reveal that the ectoine molecules penetrate the tissue within 180 min (Visualization 1).

Biomedical Optics EXPRESS

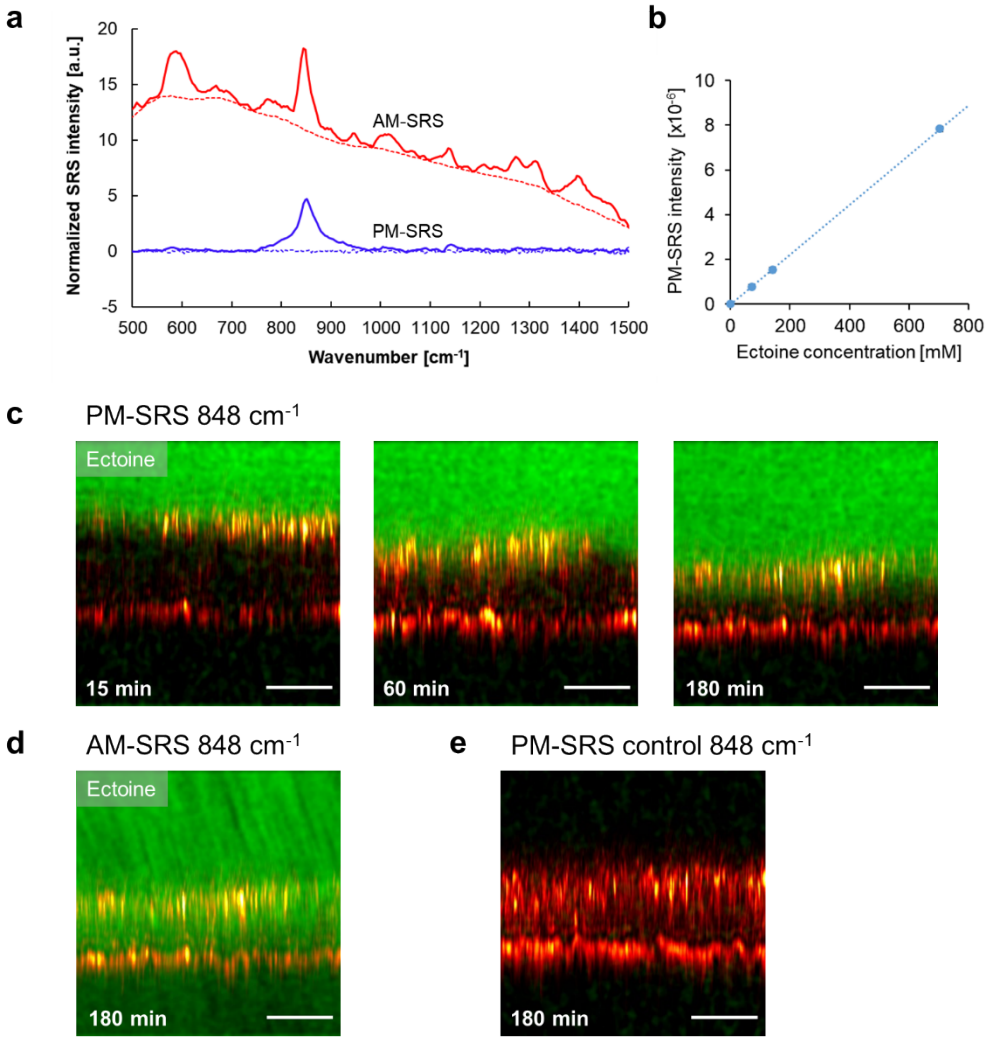

Fig. 2. SRS images of a skin moisturizing agent: (a) AM- and PM-SRS spectra of 10% ectoine solution (solid lines) and pure water (dashed lines). (b) PM-SRS versus ectoine concentration. (c-e) XZ depth images showing SRS signal intensity at 848 cm^{-1} (green) overlaid with the confocal-reflection signal (red hot) at different times after applying the ectoine solution: (c) PM-SRS at 15 min, 60 min, and 180 min (See Visualization 1), (d) AM-SRS at 180 min, and (e) PM-SRS control (no ectoine). The scale bar is 50 μm.

3.2. Label-free skin penetration analysis of topically applied drugs

Next, the developed label-free skin penetration test platform based on high-contrast SRS imaging was validated through pharmacokinetic analysis of the topically applied drugs. To evaluate the detectability of small-molecule drugs in a tissue at a low concentration, we analyzed the penetration profile of an aqueous solution of lidocaine hydrochloride (LID) and loxoprofen sodium (LOX). LID is a local anesthetic of the amide type, and LOX is a nonsteroidal anti-inflammatory drug in the propionic acid derivative group, both of which are commonly used as pain relief medicine.

Biomedical Optics EXPRESS

Prior to the penetration analysis, the spontaneous Raman spectra of the test samples and the skin tissue model were measured using a customized confocal Raman microscope with 532-nm excitation (Fig. 3(a), see Supplement 1). The corresponding PM-SRS spectra with a 1.7 ps probe delay were also measured (Fig. 3(b)). The spontaneous Raman spectrum of the skin tissue model contained congested Raman spectral lines. However, in the PM-SRS, most Raman signals from the skin tissue were suppressed by the time-resolved detection, except a narrowband peak signal at 1004 cm^{-1} (phenyl ring breathing) from the protein components. The resonant Raman peaks from cytochrome c at 750, 1130, and 1314 cm^{-1} were also suppressed due to near-infrared excitation. The PM-SRS spectra of the LID and the LOX featured their specific Raman peaks at 1092 cm^{-1} (methyl rock, CH_2 twist) and at 1184 cm^{-1} (C–C stretching), respectively. These intrinsic Raman peaks were used as signatures in the label-free skin penetration analysis.

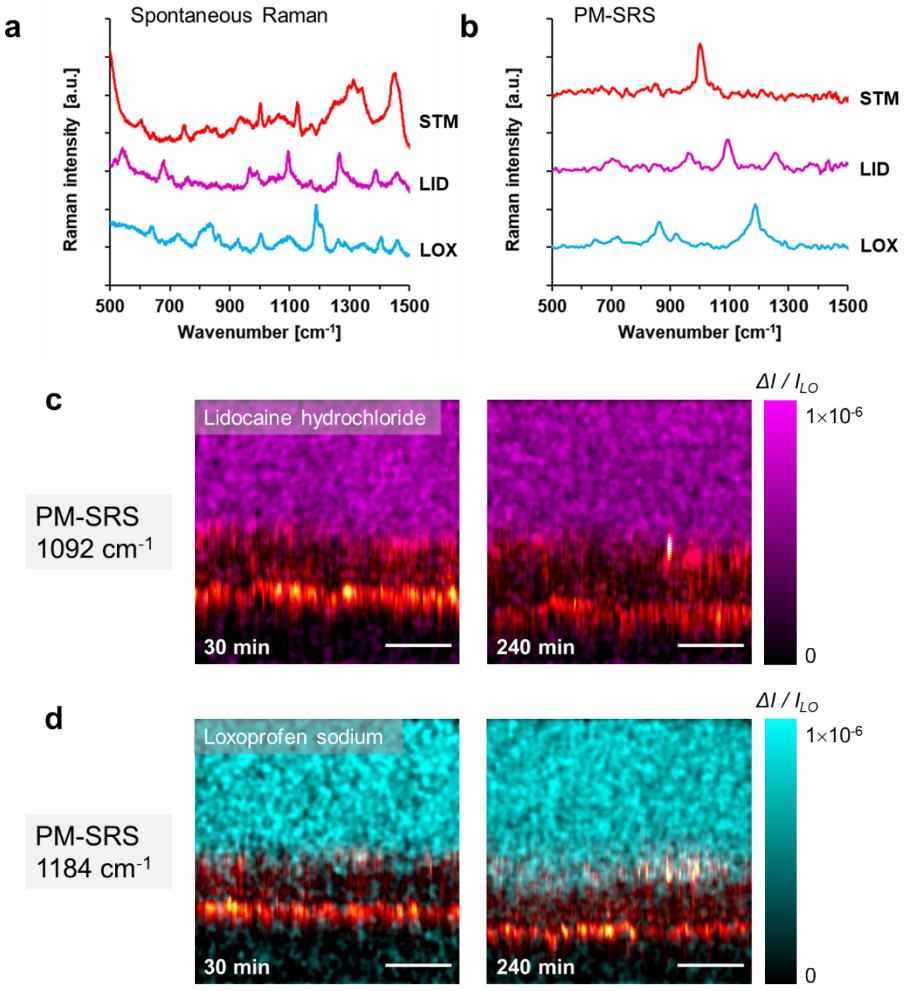

Fig. 3. Label-free skin penetration measurement of topically applied drugs: (a-b) Raman spectra of lidocaine hydrochloride (LID), loxoprofen sodium salt (LOX), and an untreated skin tissue model (STM) measured using (a) spontaneous Raman spectroscopy and (b) PM-SRS. (c-d) PM-SRS skin penetration images captured at 30 min and 240 min after applying (c) 4% LID and (d) 4% LOX solutions. The scale bar is 50 μm.

Biomedical Optics EXPRESS

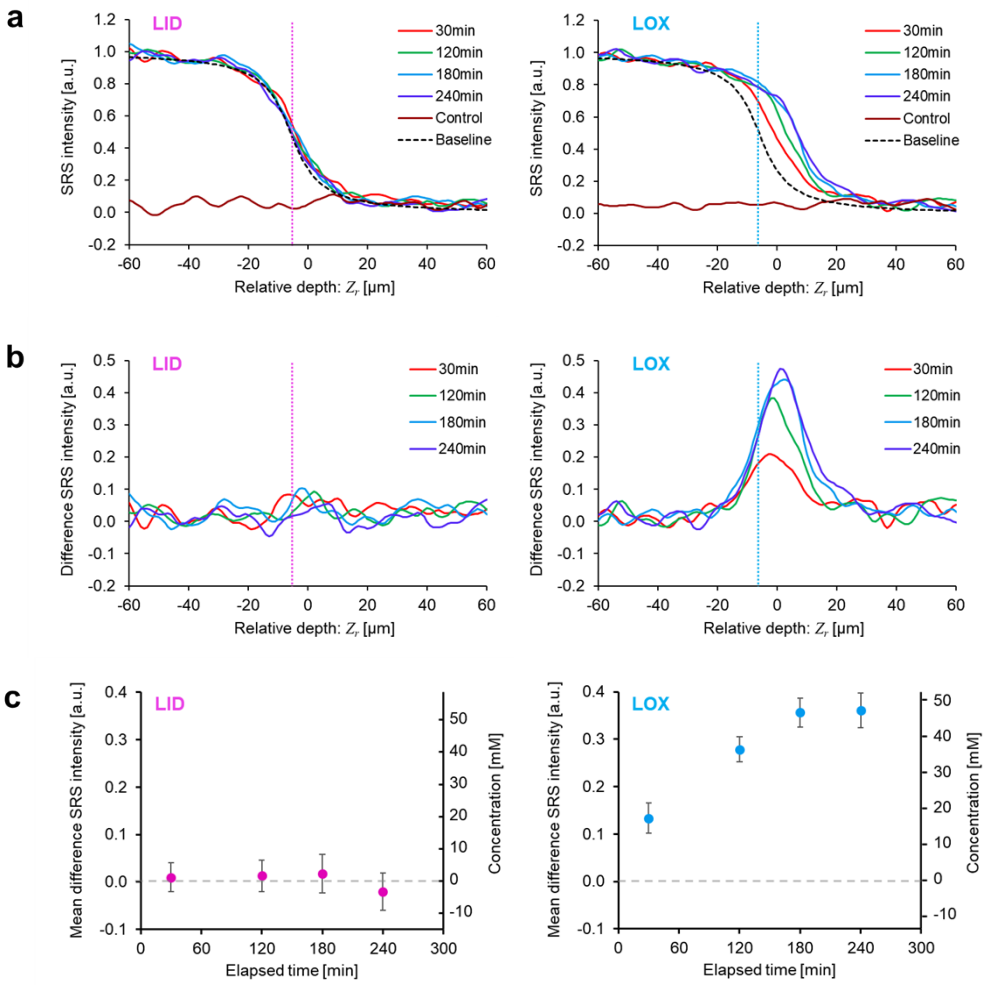

Fig. 4. Skin penetration analysis: (a) 1D PM-SRS depth profiles of the LID and the LOX with different measurement times (the negative-control profile with 0% solution is also shown), and (b) the difference depth profiles after the baseline profile was subtracted. The dotted vertical line represents the estimated top surface position of the skin tissue model. (c) Time course of the mean difference SRS intensity (averaged over the depth from −5 μm to +5 μm) in the skin tissue penetration of the drug molecules. The right vertical axis shows the corresponding millimolar concentration change. The error bars show ±2× the standard errors, representing the system noise of the SRS microscopy.

Figures 3(c) and 3(d) display the drug penetration images of 4% LID (148 mM) and 4% LOX (131 mM) acquired by the combined PM-SRS and confocal-reflection microscopy, respectively. Both SRS images provided high S/B values (LID: 22 and LOX: 17). The LID images showed no significant changes within 240 min, whereas the LOX image after 240 min depicted a spatial overlap of the SRS signal with the confocal-reflection signal at the SC layer, suggesting that the tissue is more permeable to LOX molecules.

To analyze the details of the penetration kinetics in the tissue in the low-concentration regime, the one-dimensional (1D) depth profile was calculated from the XZ image data (Fig. 4(a)), where the origin of the relative depth, Z_r, was defined as the uppermost peak position of the

Biomedical Optics EXPRESS

confocal-reflection signal profile along the Z-axis. The relative position of the tissue top surface was estimated to be $Z_r = -6$ μm (shown as dotted lines in Fig. 4(a), see Fig. S4 for details). The SRS signal intensity $\Delta I / I_{LO}$, which is proportional to the concentration, was normalized using the signal level of the donor solution (4% LID: $\Delta I / I_{LO} = 5.9 \times 10^{-7}$, 4% LOX: $\Delta I / I_{LO} = 7.7 \times 10^{-7}$). To quantify the local concentration in the tissue, the depth-dependent signal loss due to scattering was also corrected using the non-resonant background signal acquired in the PM-SRS mode with no probe time delay (Fig. S5). In the LID case, all drug depth profiles after applying the donor solution overlapped the baseline profile, where the baseline was calculated from the convolution of a Lorentzian response function and a step function (see Supplement 1). This result verifies that drug penetration was blocked at the SC surface, and there was no change in the depth profile during the measurement. In the LOX case, however, the profile shifted to the right within a few hours, thereby indicating an increase in the local drug concentration in the SC and the underlying viable cell layers.

The spatiotemporal kinetics of the drug molecules permeating the tissue barrier can be more clearly understood with the difference between the measured depth profile and baseline profile (Fig. 4(b)). The difference SRS signal profile of the LOX shows that after 240 min, the normalized SRS signal exhibits a peak at $Z_r = 1$ μm, which corresponds to an increase in the local concentration at the SC layer. Figure 4(c) shows the time course of the skin penetration of the drug samples, which was calculated from the mean difference SRS intensity averaged from −5 μm to +5 μm. The error bars represent ±2× the standard errors of the system noise obtained from each measurement. Within 240 min, the increase in the LID signal during the skin penetration could not be detected, whereas that of the LOX was clearly observed and the mean difference SRS signal reached 0.36 ± 0.04 (47.3 ± 4.8 mM) after 240 min.

Finally, we evaluated the detectability of PM-SRS drug measurements in the skin tissue model. The limit of detection is defined by the SRS signal intensity (or the sample concentration) providing a signal-to-noise ratio of 3 ($\mathrm{SNR} = S/\sigma_B = 3$), where S denotes the SRS signal in the penetration measurement, and σ_B denotes the standard error of the background SRS signals in the control measurements with pure water. Based on three times the standard errors in the control measurements of $3\sigma_B = 0.061$ ($\Delta I / I_{LO} = 4.7 \times 10^{-8}$) at 1092 cm^{-1} and $3\sigma_B = 0.037$ ($\Delta I / I_{LO} = 2.9 \times 10^{-8}$) at 1184 cm^{-1}, the limit of detections of the LID and the LOX measurements were estimated to be 9.0 mM and 4.9 mM, respectively.

4. Discussion

Previous label-free skin penetration studies using SRS microscopy have demonstrated high-speed imaging capability with high-concentration drug solution samples [11,14,15]. However, such high-concentration topical applications often lead to the crystallization of target chemicals and cell or tissue damage. By contrast, the challenges in SRS imaging at a lower concentration range (tens of mM or less) include not only the shot noise, but also a limited signal contrast due to the strong background signals from the tissue. In this study, we suppressed the background signals during tissue imaging using PM-SRS microscopy coupled with time-resolved detection, which rejects the nonlinear AM background signals and selectively detects the specific long-lived vibrational mode with shaped probe pulses. The experimental results on the penetration of ectoine into the skin model tissue clearly highlighted the superiority of PM-SRS in terms of signal contrast over conventional AM-SRS. In addition, the results of the drug penetration imaging and the depth profile analysis showed that the transport of low-concentration exogenous substances through the epidermal tissue barrier could be monitored by high-contrast PM-SRS.

Importantly, we achieved a significantly high S/B in the congested fingerprint spectral region (500–1800 cm^{-1}), despite label-free imaging. When the background signal is dominant, the output fluctuation due to the low-frequency laser noise and the concentration change during the measurement, which cannot be completely removed by the standard modulation transfer scheme

Biomedical Optics EXPRESS

[21,22], increases the measurement error σ_B. Previous successful SRS imaging experiments at lower concentration regimes have circumvented this problem using small Raman active tracers such as deuterium [23], alkynes [24], and phenyl-diyne [25], all of which lie in the cell-silent frequency region (1800–2700 cm^{-1}). However, such a Raman labeling approach requires laborious chemical modification steps for sample preparation.

Several SRS methods for suppressing the background signals have been proposed recently [18,21,22,26–33]. One approach is to acquire a broadband spectrum using multiplex SRS [26,27] or hyperspectral SRS imaging [22,28–30], followed by spectral unmixing. However, multiplex SRS involves technical difficulties owing to the need for spectroscopic optics and low-noise multichannel demodulators. Hyperspectral SRS requires a rapid frequency scanning mechanism, such as a high-speed tunable pulsed laser source [28] or a high-speed delay scanner, for tunable spectral-focusing detection [22,29,30]. In any case, additional off-resonant data acquisitions and stable control measurements are required to extract the target signal component from the multi-component background. Another simpler approach is to measure the differential output of two different SRS signals [18,21,31–33]. Among these, frequency-modulated SRS [18,21,31], which alternately scans two adjacent frequencies, works well for removing a flat spectral baseline because it functions as a first-order derivative filter in the spectral region. However, such simple filtering techniques are not always applicable; for example, when a sloping spectral background overlaps the target Raman peak, an unwanted offset is added to the differential output. Compared with existing methods, background suppression using time-resolved PM-SRS detection has two advantages: i) because it is a single-frequency SRS measurement, no high-speed frequency scanning mechanism or spectral unmixing analysis is necessary, and ii) selective enhancement of a long-lived vibration with time-asymmetric probe pulses works as a high-quality high-pass filter for spectral data; therefore, the fluctuations of the background signals from most broadband tissue components as well as the baseline offset can be excluded, facilitating quantitative measurements of the target narrowband signals even in the millimolar concentration regime.

With PM-SRS, the detection limits of the topically applied drugs in the skin tissue model were in the order of millimolar. For reference, the SRS signal of the LOX at the detection limit ($\Delta I / I_{LO} = 2.9 \times 10^{-8}$ at 1184 cm^{-1}, with a 1.7-ps probe delay) corresponds to the concentrations of 0.75 mM caffeine at 562 cm^{-1} and 1.0 mM dimethyl sulfoxide at 678 cm^{-1} aqueous solutions, respectively (these are standard substances used in previous skin penetration studies [11,34]). The improved detectability enables the assessment of skin penetration at a practical concentration range, and the measurement of less soluble drugs that could not be measured using conventional SRS while avoiding potential crystallization and tissue damage.

While many previous studies have demonstrated time-resolved coherent Raman spectroscopy and microscopy [35–38], their potential in low-concentration chemical measurements has not been fully explored. Our results are the first demonstration that clearly showcases the real power and utility of the time-resolved method in drug imaging applications. The key to the successful implementation of the PM-SRS is engineered pulse shaping, which enables high-contrast SRS signal detection in the cellular-silent temporal region. Our time-domain optical design approach offers a new avenue for breaking the detectability limit of label-free coherent Raman microscopy. A common limitation in time-resolved signal detection is that it requires a narrowband Raman peak (or a long vibrational coherence lifetime) to achieve a high S/B. Fortunately, however, most small-molecule active compounds and drugs used in dermatology, pharmaceuticals, and cosmetics have a defined structure, providing sharp and well-differentiated Raman peak patterns [7], as shown in the experiment. This suggests that time-resolved PM-SRS can be used in various biomedical applications.

Notably, there are additional uncertainties in the results presented here. Although *in vitro* skin models generally provide better reproducibility than *ex vivo* and *in vivo* human skin studies, their penetration kinetics could vary depending on parameters such as the culture conditions and

Biomedical Optics EXPRESS

heterogeneity of the samples. Therefore, a well-designed assessment plan with an increased sample number is necessary to discuss the penetration characteristics in more detail. In addition, the drug penetration properties of cultured skin tissue models differ from those of human skin tissues. Experimental verification using human skin samples is currently underway.

5. Conclusion

We present a skin penetration analysis technique using high-contrast depth-resolved imaging based on label-free SRS microscopy. By enhancing the intrinsic vibrational signal contrast of long-lived Raman modes using pulse-shaping technology, PM-SRS microscopy provides an unprecedented detectability of small-molecule substances in tissue imaging. A proof-of-concept experiment with a topically applied skin moisturizing agent in an *in vitro* skin tissue model revealed that PM-SRS yields Raman signal contrast 40 times higher than that of AM-SRS in the spectral fingerprint region. Moreover, a drug penetration measurement with depth profile analysis has shown that PM-SRS microscopy can be used to monitor the spatial and temporal pharmacokinetics of therapeutic drugs in the millimolar concentration regime in a tissue. With the enhanced detectability, this new label-free SRS microscopy will provide opportunities to advance our understanding of skin biology, accelerate the development of new formulations and cosmetic products, and study the physiological effects of small-molecule drugs. Furthermore, we envision that the developed imaging platform to analyze drug penetration through a tissue barrier will also be applicable to other *in vitro* and *ex vivo* tissue models for early-stage drug screening. Ultimately, it may also be applied to *in vivo* imaging for drug monitoring applications.

Funding. Program on Open Innovation Platform with Enterprises, Research Institute and Academia (JPMJOP1833); Japan Society for the Promotion of Science (JP18H01895).

Acknowledgements. The authors thank Dr. Yuki Obara, Kazuyuki Iwaikawa, Yu Okano, and Masahiro Ikejiri for assisting with the spontaneous Raman spectroscopy, and Dr. Ying-Kuan Ko for helping us design the optical setup. The authors acknowledge Masumi Hayashi for supporting the development of the microscope. This research was funded by Matsumoto Trading Co., Ltd.

Disclosures. TI and KM: Tokyo University of Agriculture and Technology (P), RI, YN, and TO: Matsumoto Trading Co., Ltd. (E).

Data availability. Data underlying the results presented in this paper are not publicly available at this time but may be obtained from the authors upon reasonable request.

Supplemental document. See Supplement 1 for supporting content.

References

1. C. Herkenne, I. Alberti, A. Naik, Y. N. Kalia, F. X. Mathy, V. Préat, and R. H. Guy, "In vivo methods for the assessment of topical drug bioavailability," Pharm. Res. **25**(1), 87–103 (2008).
2. B. Godin and E. Touitou, "Transdermal skin delivery: Predictions for humans from in vivo, ex vivo and animal models," Adv. Drug Delivery Rev. **59**(11), 1152–1161 (2007).
3. R. Darlenski, S. Sassning, N. Tsankov, and J. W. Fluhr, "Non-invasive in vivo methods for investigation of the skin barrier physical properties," Eur. J. Pharm. Biopharm. **72**(2), 295–303 (2009).
4. J. Lademann, U. Jacobi, C. Surber, H. J. Weigmann, and J. W. Fluhr, "The tape stripping procedure – Evaluation of some critical parameters," Eur. J. Pharm. Biopharm. **72**(2), 317–323 (2009).
5. L. Bartosova and J. Bajgar, "Transdermal drug delivery in vitro using diffusion cells," Curr. Med. Chem. **19**(27), 4671–4677 (2012).
6. P. J. Caspers, G. W. Lucassen, E. A. Carter, H. A. Bruining, and G. J. Puppels, "In vivo confocal Raman microspectroscopy of the skin: Noninvasive determination of molecular concentration profiles," J. Invest. Dermatol. **116**(3), 434–442 (2001).
7. L. Franzen and M. Windbergs, "Applications of Raman spectroscopy in skin research - From skin physiology and diagnosis up to risk assessment and dermal drug delivery," Adv. Drug Delivery Rev. **89**, 91–104 (2015).
8. A. Zumbusch, G. R. Holtom, and X. S. Xie, "Three-dimensional vibrational imaging by coherent anti-Stokes Raman scattering," Phys. Rev. Lett. **82**(20), 4142–4145 (1999).
9. C. L. Evans and X. S. Xie, "Coherent anti-Stokes Raman scattering microscopy: chemically imaging for biology and medicine," Annu. Rev. Anal. Chem. **1**(1), 883–909 (2008).
10. X. Chen, S. Grégoire, F. Formanek, J. B. Galey, and H. Rigneault, "Quantitative 3D molecular cutaneous absorption in human skin using label free nonlinear microscopy," J. Controlled Release **200**, 78–86 (2015).

Biomedical Optics EXPRESS

11. C. W. Freudiger, W. Min, B. G. Saar, S. Lu, G. R. Holtom, C. He, J. C. Tsai, J. X. Kang, and X. S. Xie, "Label-free biomedical imaging with high sensitivity by stimulated Raman scattering microscopy," Science **322**(5909), 1857–1861 (2008).
12. Y. Ozeki, F. Dake, S. Kajiyama, K. Fukui, and K. Itoh, "Analysis and experimental assessment of the sensitivity of stimulated Raman scattering microscopy," Opt. Express **17**(5), 3651–3658 (2009).
13. P. Nandakumar, A. Kovalev, and A. Volkmer, "Vibrational imaging based on stimulated Raman scattering microscopy," New J. Phys. **11**(3), 033026 (2009).
14. B. G. Saar, L. R. Contreras-Rojas, X. S. Xie, and R. H. Guy, "Imaging drug delivery to skin with stimulated Raman scattering microscopy," Mol. Pharmaceutics **8**(3), 969–975 (2011).
15. N. A. Belsey, N. L. Garrett, L. R. Contreras-Rojas, A. J. Pickup-Gerlaugh, G. J. Price, J. Moger, and R. H. Guy, "Evaluation of drug delivery to intact and porated skin by coherent Raman scattering and fluorescence microscopies," J. Controlled Release **174**, 37–42 (2014).
16. J. X. Cheng, "Coherent anti-Stokes Raman scattering microscopy," Appl. Spectrosc. **61**(9), 197A–208A (2007).
17. D. Zhang, P. Wang, M. N. Slipchenko, and J. X. Cheng, "Fast vibrational imaging of single cells and tissues by stimulated Raman scattering microscopy," Acc. Chem. Res. **47**(8), 2282–2290 (2014).
18. D. Zhang, M. N. Slipchenko, D. E. Leaird, A. M. Weiner, and J. X. Cheng, "Spectrally modulated stimulated Raman scattering imaging with an angle-to-wavelength pulse shaper," Opt. Express **21**(11), 13864–13874 (2013).
19. T. Ito, Y. Obara, and K. Misawa, "Single-beam phase-modulated stimulated Raman scattering microscopy with spectrally focused detection," J. Opt. Soc. Am. B **34**(5), 1004–1015 (2017).
20. T. Ito, Y. Obara, and K. Misawa, "Spectral focusing with asymmetric pulses for high-contrast pump–probe stimulated Raman scattering microscopy," APL Photonics **3**(9), 092405 (2018).
21. D. Fu, W. Yang, and X. S. Xie, "Label-free imaging of neurotransmitter acetylcholine at neuromuscular junctions with stimulated Raman scattering," J. Am. Chem. Soc. **139**(2), 583–586 (2017).
22. R. He, Z. Liu, Y. Xu, W. Huang, H. Ma, and M. Ji, "Stimulated Raman scattering microscopy and spectroscopy with a rapid scanning optical delay line," Opt. Lett. **42**(4), 659–662 (2017).
23. A. Alfonso-García, S. G. Pfisterer, H. Riezman, E. Ikonen, and E. O. Potma, "D38-cholesterol as a Raman active probe for imaging intracellular cholesterol storage," J. Biomed. Opt. **21**(6), 061003 (2015).
24. L. Wei, F. Hu, Y. Shen, Z. Chen, Y. Yu, C. C. Lin, M. C. Wang, and W. Min, "Live-cell imaging of alkyne-tagged small biomolecules by stimulated Raman scattering," Nat. Methods **11**(4), 410–412 (2014).
25. H. J. Lee, W. Zhang, D. Zhang, Y. Yang, B. Liu, E. L. Barker, K. K. Buhman, L. V. Slipchenko, M. Dai, and J. X. Cheng, "Assessing cholesterol storage in live cells and C. elegans by stimulated Raman scattering imaging of phenyl-diyne cholesterol," Sci. Rep. **5**(1), 7930 (2015).
26. K. Seto, Y. Okuda, E. Tokunaga, and T. Kobayashi, "Multiplex stimulated Raman imaging with white probe-light from a photonic-crystal fibre and with multi-wavelength balanced detection," J. Phys. D: Appl. Phys. **47**(34), 345401 (2014).
27. [27] C. S. Liao, M. N. Slipchenko, P. Wang, J. Li, S. Y. Lee, R. A. Oglesbee, and J. X. Cheng, "Microsecond scale vibrational spectroscopic imaging by multiplex stimulated Raman scattering microscopy," Light: Sci. Appl. **4**(3), e265 (2015).
28. Y. Ozeki, W. Umemura, Y. Otsuka, S. Satoh, H. Hashimoto, K. Sumimura, N. Nishizawa, K. Fukui, and K. Itoh, "High-speed molecular spectral imaging of tissue with stimulated Raman scattering," Nat. Photonics **6**(12), 845–851 (2012).
29. C.-S. Liao, K.-C. Huang, W. Hong, A. J. Chen, C. Karanja, P. Wang, G. Eakins, and J.-X. Cheng, "Stimulated Raman spectroscopic imaging by microsecond delay-line tuning," Optica **3**(12), 1377–1380 (2016).
30. D. Fu, J. Zhou, W. S. Zhu, P. W. Manley, Y. K. Wang, T. Hood, A. Wylie, and X. S. Xie, "Imaging the intracellular distribution of tyrosine kinase inhibitors in living cells with quantitative hyperspectral stimulated Raman scattering," Nat. Chem. **6**(7), 614–622 (2014).
31. H. Xiong, N. Qian, Z. Zhao, L. Shi, Y. Miao, and W. Min, "Background-free imaging of chemical bonds by a simple and robust frequency-modulated stimulated Raman scattering microscopy," Opt. Express **28**(10), 15663–15677 (2020).
32. P. Berto, E. R. Andresen, and H. Rigneault, "Background-free stimulated Raman spectroscopy and microscopy," Phys. Rev. Lett. **112**(5), 053905 (2014).
33. M. Andreana, M. A. Houle, D. J. Moffatt, A. Ridsdale, E. Buettner, F. Légaré, and A. Stolow, "Amplitude and polarization modulated hyperspectral stimulated Raman scattering microscopy," Opt. Express **23**(22), 28119–28131 (2015).
34. L. Franzen, J. Anderski, and M. Windbergs, "Quantitative detection of caffeine in human skin by confocal Raman spectroscopy–A systematic in vitro validation study," Eur. J. Pharm. Biopharm. **95**(A), 110–116 (2015).
35. M. Yoshizawa and M. Kurosawa, "Femtosecond time-resolved Raman spectroscopy using stimulated Raman scattering," Phys. Rev. A **61**(1), 013808 (1999).
36. A. Volkmer, L. D. Book, and X. S. Xie, "Time-resolved coherent anti-Stokes Raman scattering microscopy: Imaging based on Raman free induction decay," Appl. Phys. Lett. **80**(9), 1505–1507 (2002).
37. N. Dudovich, D. Oron, and Y. Silberberg, "Single-pulse coherently controlled nonlinear Raman spectroscopy and microscopy," Nature **418**(6897), 512–514 (2002).

Biomedical Optics EXPRESS

38. M. Cui, M. Joffre, J. Skodack, and J. P. Ogilvie, "Interferometric Fourier transform coherent anti-stokes Raman scattering," Opt. Express **14**(18), 8448–8458 (2006).